A new code for predicting the thermo-mechanical and irradiation behavior of metallic fuels in sodium fast reactors

Aydın Karahan *, Jacopo Buongiorno

Center for Advanced Nuclear Energy Systems, Nuclear Science and Engineering Department, Massachusetts Institute of Technology, United States

ARTICLE INFO

ABSTRACT

An engineering code to predict the irradiation behavior of U–Zr and U–Pu–Zr metallic alloy fuel pins and UO_2–PuO_2 mixed oxide fuel pins in sodium-cooled fast reactors was developed. The code was named Fuel Engineering and Structural analysis Tool (FEAST). FEAST has several modules working in coupled form with an explicit numerical algorithm. These modules describe fission gas release and fuel swelling, fuel chemistry and restructuring, temperature distribution, fuel–clad chemical interaction, and fuel and clad mechanical analysis including transient creep-fracture for the clad. Given the fuel pin geometry, composition and irradiation history, FEAST can analyze fuel and clad thermo-mechanical behavior at both steady-state and design-basis (non-disruptive) transient scenarios.

FEAST was written in FORTRAN-90 and has a simple input file similar to that of the LWR fuel code FRAPCON. The metal–fuel version is called FEAST-METAL, and is described in this paper. The oxide–fuel version, FEAST-OXIDE is described in a companion paper. With respect to the old Argonne National Laboratory code LIFE-METAL and other same-generation codes, FEAST-METAL emphasizes more mechanistic, less empirical models, whenever available. Specifically, fission gas release and swelling are modeled with the GRSIS algorithm, which is based on detailed tracking of fission gas bubbles within the metal fuel. Migration of the fuel constituents is modeled by means of thermo-transport theory. Fuel–clad chemical interaction models based on precipitation kinetics were developed for steady-state operation and transients. Finally, a transient intergranular creep-fracture model for the clad, which tracks the nucleation and growth of the cavities at the grain boundaries, was developed for and implemented in the code. Reducing the empiricism in the constitutive models should make it more acceptable to extrapolate FEAST-METAL to new fuel compositions and higher burnup, as envisioned in advanced sodium reactors.

FEAST-METAL was benchmarked against the open-literature EBR-II database for steady state and furnace tests (transients). The results show that the code is able to predict important phenomena such as clad strain, fission gas release, clad wastage, clad failure time, axial fuel slug deformation and fuel constituent redistribution, satisfactorily.

1. Introduction

Sodium-cooled fast reactors (SFR) have regained worldwide interest in recent years thanks to international programs such as generation-IV [1] and the Global Nuclear Energy Partnership (GNEP) [2]. The success of these reactors in accomplishing their mission of energy production and improved actinide management, while attaining competitive economics, will largely depend upon the ability of their fuel to operate reliably at high burnup, power density and plant thermal efficiency. The primary fuel candidates for sodium reactors are oxide and metal fuels. In these systems, the clad operates at high peak clad temperature (>600 °C), fast neutron flux (>10^{15} n/cm^2), and stresses (>100 MPa); in this aggressive environment, various thermo-chemico-mechanical phenomena

such as clad thermal and irradiation creep and void swelling, clad wastage, and fuel–clad mechanical interaction may limit the achievable burnup, the core power density and the reactor operating temperatures. Therefore, predicting the behavior of the fuel is a critical objective in fast reactors design and analysis. At MIT we have been developing a new fuel performance code to achieve this objective. The code was named Fuel Engineering and Structural analysis Tool, or FEAST, and comes in two versions: FEAST-METAL for the analysis of metal fuels, and FEAST-OXIDE for the analysis of oxide fuels. This paper describes FEAST-METAL, while FEAST-OXIDE is described in a companion paper.

2. Background and motivation

A metal fuel pin is conceptually a simple object, its basic parts being a cylindrical slug of the metal alloy of interest, e.g., U–Pu–Zr, encased in a clad tube, made of a low-swelling stainless steel,

---

* Corresponding author. Tel.: +1 617 258 0752.
  E-mail address: karahan@mit.edu (A. Karahan).

e.g., HT 9. Addition of some zirconium (~10% by weight) to the U–Pu alloy raises the solidus temperature of the fuel and prevents fuel–clad interdiffusion at temperatures typical of steady operating conditions [3]. The gap between the fuel slug and the clad is filled with liquid sodium, which functions as a thermal bond. A certain free volume, called the gas plenum, is provided above the fuel slug to relieve the pressure due to fission gas release from the fuel during irradiation. The gas plenum is usually pre-filled with helium at near-atmospheric pressure. The attractive characteristics of metal fuel include (i) a high thermal conductivity, which combined with a highly conducting gap, maintains fuel temperatures low and reduces stored energy, an important feature during transients, such as the unprotected loss of primary flow and loss of heat sink, (ii) high heavy metal density and low moderating power, which provide for a harder spectrum and excellent neutron economy, (iii) good compatibility with the sodium coolant, and (iv) ease of manufacturing and reprocessing by pyrochemical methods.

Although metal fuel has many attractive properties, its poor chemical stability with the cladding material above 650 °C (U–19Pu–10Zr/HT 9) limits the operating reactor temperature and thus the plant thermal efficiency. Furthermore, the possibility of surviving in long transient scenarios (on the order of days) and above the fuel clad liquefaction temperature is very low. Finally, note that operating with an excessively hard neutron spectrum may require a much more irradiation resistant cladding material than the ferritic–martensitic alloys currently considered, if a reasonably high discharge burnup is to be achieved.

The in-core performance of metal fuels is limited by various thermo-chemico-mechanical phenomena. For a typical U–19Pu–10Zr fuel pin, the metal fuel slug undergoes significant swelling upon irradiation, due to the generation of the fission gases. Fuel–clad contact occurs within 1–2 at.% peak burnup at operating conditions typical of EBR-II [4]. At this time the fuel and clad are 'locked' both axially and radially, in the upper section of the fuel. The fuel in this region is hot and rather compliant (the dominant phase being single γ phase). It could be possible to control the thermal creep level by only adjusting the gas plenum height. On the other hand, the middle and lower regions of the fuel are colder and stiffer (($\alpha + \delta$) phase fraction is significant here). However, Fuel/Clad Mechanical Interaction (FCMI) remains moderately low throughout the fuel thanks to fission gas-bubble interconnection and the associated release of the fission gases into the plenum. For typical 72% smear-density EBR-II fuel and operating conditions, this benign situation persists up to 13–15 at.%, beyond which the accumulation of solid-fission products stiffens the fuel slug; thus FCMI begins to rise significantly until clad failure occurs due to embrittlement by irradiation creep. If the magnitude of the fast neutron flux is high or the neutron spectrum is excessively hard, the dose to the clad may induce void swelling at high burnup, resulting in further embrittlement of the clad. Clad embrittlement may lead to trans-granular creep fracture [5]. During transients, the situation is different. Due to the strong temperature dependency of thermal creep, the critical region in the fuel shifts from the peak power point (typically at mid-plane) to the top region, where the clad is hottest. In this situation, intergranular creep fracture of the clad becomes the most probable failure mechanism. Furthermore, during transients, one has to guard against Fuel/Clad Chemical Interaction (FCCI), which may result in the formation of low-melting eutectics that waste the clad [6]. It is clear from this brief discussion that any credible attempt at assessing the performance of metal fuel must include models that are able to predict the time-dependent temperature, stress and strain distribution and micro-structural evolution within the clad and fuel for given operating and abnormal conditions. These models should include the effects of fission gas release, fuel swelling and creep, FCMI, thermal expansion, clad

thermal and irradiation creep and swelling, fuel restructuring, FCCI and clad failure.

Several metal fuel performance codes have been developed to date. A summary of their capabilities is given in Table 1. Note that in all cases the overall code structure consists of several modules describing the important individual phenomena, numerically coupled to predict the integral behavior of the fuel.

It was decided to develop a new metal fuel code, FEAST-METAL, for the following reasons:

  - The older codes (LIFE-METAL [7] and SESAME [8]) are highly empirical and cannot be extrapolated beyond the narrow database for which they were developed. This is a severe limitation as there is a growing interest in new metal fuel alloys and higher burnup levels, particularly for transmutation of the transuranic elements [11].
  - There is a need for a robust code for analysis of fuel behavior during transients.
  - Regulators will need an independent tool to verify the performance of metal fuel for next-generation of fast reactors.
  - The newer codes being developed in Asia (ALFUS [9] and MACSIS [10]) may not become available to researchers/vendors/regulators in US.

FEAST-METAL was developed to be flexible, so that constitutive models for non-traditional metal alloys (e.g., TRU–Zr) can be easily added to the code. Other attractive features of FEAST-METAL include the ability to account for the variation of material properties (fuel creep, thermal expansion, Young's modulus) with phases present, a mechanistic fission gas release and swelling model originally developed for metal fuel, a FCCI model based on precipitation kinetics, a fuel constituent redistribution model based on thermo-transport theory, a thermal conductivity model that accounts for the effect of porosity as well as sodium-bond infiltration [12] and fuel constituent redistribution, and a transient clad creep-fracture model based on the constrained diffusional cavity growth mechanism. The 'philosophy' behind the development of FEAST-METAL was to create an engineering continuum-level code by using and improving on the most advanced mechanistic models, whenever possible. There is currently interest in the US and Europe to develop a multi-scale fuel behavior code system including atomistic, meso-scale and macroscopic approaches in coupled form. A preliminary attempt at the meso-scale level modeling is reported in Ref. [13]. Such a high fidelity and coupled approach is expected not to be ready soon. In the meantime there is a need for a robust and reliable code to (i) guide the development of advanced metal fuels, and be used in (ii) pre-irradiation calculations and (iii) scoping studies of novel fast reactors.

In FEAST-METAL the fuel and clad regions can be divided into up to eight radial nodes each. The number of axial nodes is also user specified, and can be at most twenty. The code was written in FORTRAN-90 program language. It has a simple input file that is structured like the input file of the LWR oxide fuel code FRAPCON [14]. The user must specify the fuel pin geometry, composition and operating conditions (coolant inlet temperature and mass flow rate, axial power distribution, fast neutron flux and flux-to-dose conversion factor); for transients, the transient starting time and the operating conditions throughout the event must also be specified by the user. The code implements an explicit numerical algorithm and couples the models describing the relevant physical phenomena. The flow sheet of the calculations is given in Fig. 1. The Gauss–Jordan matrix solver algorithm [15] was adopted in the solution of the mechanical-equilibrium equation and heat equation. Note that the very high rate of creep strain of the fuel slug requires short time steps, of the order of 10–20 s; therefore a typical irradiation simulation requires use of about

Table 1
Metallic fuel performance codes.

	LIFE-METAL [7]	SESAME [8]	ALFUS [9]	MACSIS [10]	FEAST-METAL
Developer	ANL (US)	CRIEPI (JAPAN)	CRIEPI (JAPAN)	KAERI (Korea)	MIT (US)
General Capabilities	Steady-state and transient behavior	Steady-state behavior	Steady-state behavior	Steady-state behavior	Steady-state and transient behavior
Fission gas release and fuel swelling	Empirical correlation	Empirical correlation	Mechanistic model, based on UO_2 Fuel	Mechanistic model, based on UO_2 fuel	Mechanistic model, based on metallic fuel
Constituent redistribution	Empirical correlation	Chemical equilibrium model	Thermo-transport theory	Thermo-transport theory	Thermo-transport theory
Temperature distribution	1D model	1D model	1D model	1D model	1D model
Mechanical analysis	1D model	1D model	2D model	1D model	1D model
FCCI	Empirical correlation	Not included	Empirical correlation	Not included	Diffusion model based on precipitation kinetics
Creep fracture	Cumulative damage fraction model	N/A	N/A	N/A	(1) Cumulative Damage Fraction Model (2) Constrained Diffusional Cavity Growth Model

10^6 time steps, resulting in an execution time of the order of minutes, when run on a single CPU personal computer.

The main modules of FEAST-METAL are briefly described in Sections 3–7; the validation effort is discussed in Section 8. The conclusions are provided in Section 9. A detailed description of FEAST-METAL can be found in [16].
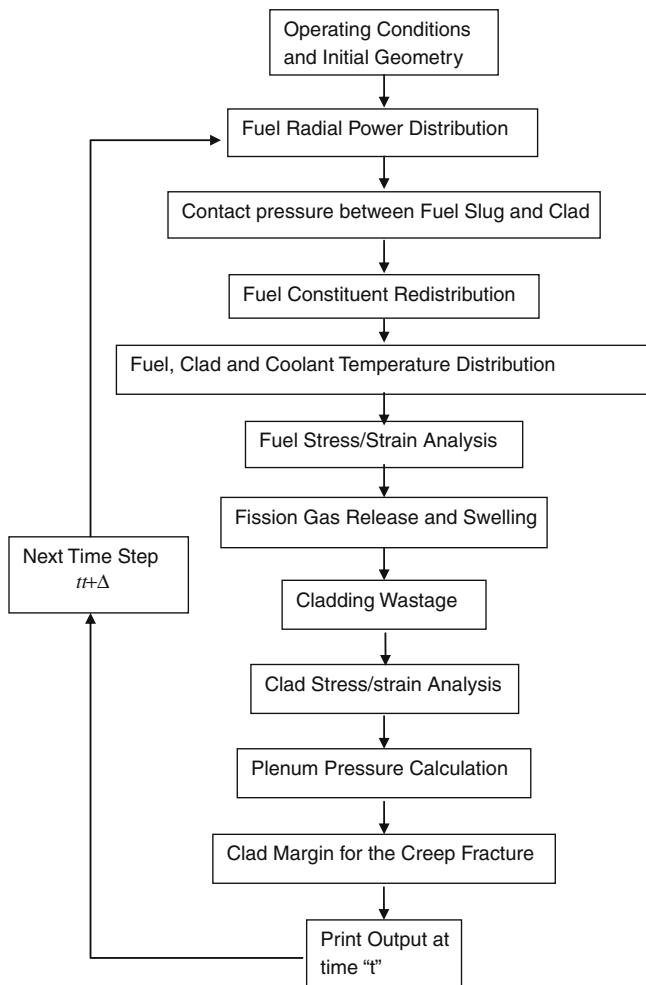

Fig. 1. Flow sheet of FEAST-METAL.

3. Fission gas release and swelling

The GRSIS model [17] was adopted to predict the fission gas behavior of metal fuels. A schematic diagram of the GRSIS approach is shown in Fig. 2. Fission gas atoms are generated by fission and then form (nucleate) new bubbles or diffuse into existing bubbles. The bubbles are assumed to nucleate uniformly in the metallic fuel matrix, since nucleation can occur at both the grain boundaries and the phase boundaries, which are randomly distributed inside the grain. The closed bubbles can grow by diffusion of newly created fission gas atoms, and are classified into two groups depending on their sizes. Small bubbles and large bubbles are defined as having ~0.5 and ~10 μm radius, respectively, based on post irradiation examination results given in Ref. [4]. The third group of bubbles is the open bubbles (or open pores), which are connected to each other and open to the gas plenum. When a closed bubble-i becomes an open bubble, it is assumed to be transformed into bubble-3i. Open pore formation and fission gas release into the plenum is assumed to start when the fuel matrix swelling due to the closed bubbles reaches a threshold value (10%) [9].

The same form of the bubble rate equations given in Ref. [17] was adopted in FEAST-METAL; however, two improvements have been made in the bubble growth and coalescence models, as described next. If the number density of bubble-j is N_{bj}, the average distance between bubble-j's, calculated assuming the bubbles are arranged according to a faced-centered cubic (fcc) lattice, is:

$$l_j = 1.122 N_{bj}^{-1/3} \quad (m) \tag{1}$$

Then, when there is a bubble-i in the space where bubble-j's are evenly distributed at the number density, the average distance between the centers of bubble-i and bubble-j becomes $0.5l_j$ which we calculated by means of a simple Monte Carlo simulation of randomly distributed bubbles in 3D space. Note that Ref. [17] recommended using $0.25l_j$ for the average distance between the centers of bubble-i's, which was based on an incorrect 2D calculation.

The second change with respect to the original GRSIS model pertains to the bubble coalescence. The probability per unit time of a bubble-i colliding with a bubble-j due to radial growth of bubble-i, P_{ij}, is

$$P_{ij} = \frac{\text{radial growth of bubble-}i}{\text{distance between the surfaces of bubble-}i \text{ and } j}$$

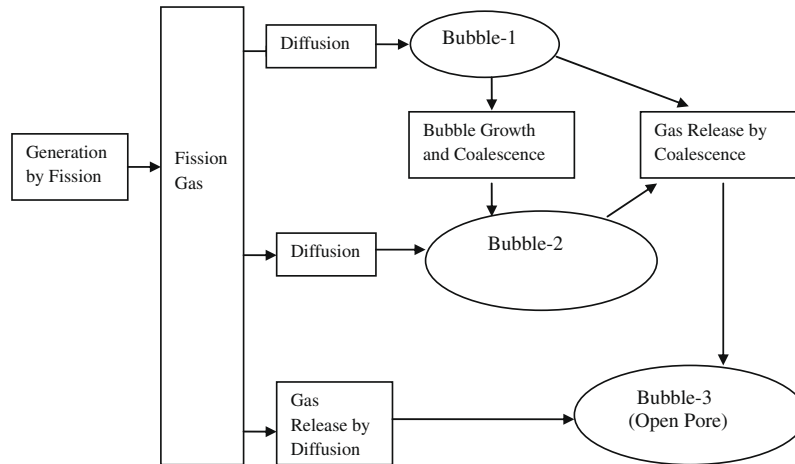$$= \frac{dr_{bi}/dt}{0.5l_j - (r_{bi} + r_{bj})} \quad (1/s) \tag{2}$$

Fig. 2. Fission gas and bubble evolution model.

where Δr_{bi} is the growth rate of bubble-i (m/s), r_{bi} the radius of bubble-i (m), and r_{bj} the radius of bubble-j (m). Eq. (2) was modified in FEAST-METAL, only for the collision between a closed bubble-i and an open bubble-j, as follows:

$$P_{ij} = \frac{d_{rbi}/dt}{d_1 l_j} \tag{3}$$

thus, it was assumed that the collision probability is proportional to the radial growth of bubble-i and inversely proportional to the average distance between two open bubble-j's; d_1 is the open porosity formation factor, newly introduced in this study and its value is 0.235.

In addition to porosity, gas diffusion also plays an important role in the simulation. The diffusion coefficient is assumed to depend on temperature according to an Arrhenius-type relation:

$$D = D_o \exp\left(-\frac{Q}{RT}\right) \tag{4}$$

where the value of the activation energy, Q, was taken to be 52000 cal/g mol, as per Ref. [18], while the value recommended in Ref. [17] was discarded as it led to an overestimation of the fission gas release and swelling at the lower temperatures [16]. The diffusion constant, D_o, was left as a fitting parameter, its value is 2.3×10^{-3} m^2/s.

Open porosity formation factor and gas diffusion constant have been fitted to EBR-II X430 fuel assembly post irradiation examination results. The predictions are given in the steady state benchmarking section (Section 8).

4. Fuel constituent redistribution

Fuel constituent redistribution is driven by the migration of Zr atoms, which is due to the chemical activity gradients associated with the multiple crystalline phases of the fuel alloy, created by the radial temperature distribution. Fuel constituent redistribution affects the fuel slug material physical properties (e.g., solidus and liquidus temperatures, thermal conductivity, specific heat), its mechanical properties (e.g., modulus of elasticity), the FCCI, and the radial power density profile. Upon constituent redistribution, the microstructure of metal fuel exhibits three distinct concentric zones, a Zr-enriched central zone (single γ phase), a Zr-depleted U-enriched intermediate zone ($\beta + \gamma$ phase), and a Zr-enriched zone on the outer periphery ($\alpha + \delta$ phase) [19]. In analyzing fuel redistribution, the following assumptions were made [19,20]:

- Pu is immobile. Therefore, the equilibrium phases of the ternary U–Zr–Pu alloy are described by using a quasi-binary U–Zr diagram with constant Pu content.
- The minimum allowed Zr concentration in the Zr-depleted central region is 5 at.% due to the solubility limit.
- Only radial Zr migration is considered.
- Cross-terms, relating the flux of one species to the chemical potential gradient of another species in the constitutive equations are negligible.

The phase diagrams, diffusion coefficients, enthalpy of solution and effective heats of transport of Zr and U in the ternary alloy are the fundamental data required by the fuel redistribution model, and were taken from Refs. [19–22]. See the appendix for the numerical values of the fundamental data. Fig. 3 shows a generic pseudo-binary phase diagram for U–Pu–Zr alloys. The solubility lines 1 through 6 are linearly interpolated between U–Zr and U–19Pu–Zr fuels using the databases provided in [22,19], respectively. The model is based on thermo-transport theory. Within a single γ-phase region the Zr interdiffusion flux, J_{Zr} (mol/m^{2}s), is given as

$$J_{Zr} = -D_{Zr}^{eff}\left(\frac{\partial C_{Zr}}{\partial r} + \frac{Q_{Zr} C_{Zr}}{RT^2}\frac{\partial T}{\partial r}\right) \tag{5}$$

where C_{Zr} is the Zr concentration (mol/m^3), D_{Zr}^{eff} the effective Zr interdiffusion coefficient in the γ-phase (m^2/s), Q_{Zr} the Zr heat of transport in the γ-phase (J/mol), R the universal gas constant (8.314 J/mol K), and the T the local fuel temperature (K). Within a
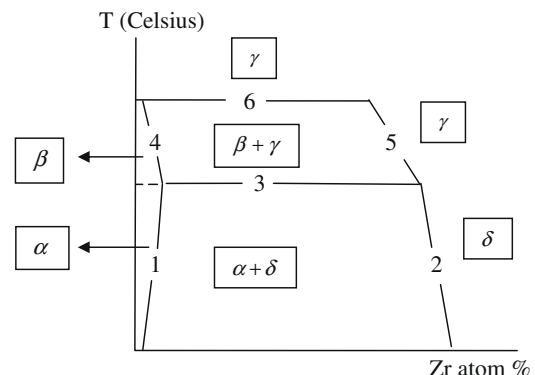

Fig. 3. Pseudo binary phase diagram for U–Pu–Zr fuel for fixed Pu content.

dual-phase region, such as $\alpha + \delta$ and $\beta + \gamma$, the Zr interdiffusion flux is expressed as

$$J_{Zr} = -V_1 D_{Zr,1}^{eff} C_{Zr,1} \frac{\Delta\overline{H}_{s,1} + Q_{Zr,1}}{RT^2} \frac{\partial T}{\partial r} - V_2 D_{Zr,2}^{eff} C_{Zr,2} \frac{\Delta\overline{H}_{s,2} + Q_{Zr,2}}{RT^2}$$
$$\times \frac{\partial T}{\partial r} \tag{6}$$

where V is the volume fraction of one phase, and $\Delta\overline{H}_s$ is the enthalpy of solution (J/mol), while the subscripts '1' and '2' indicate the first and second phase respectively. Note that in Eq. (5) (single phase), the concentration gradient appears explicitly, whereas in Eq. (6) (dual phases), the concentration of zirconium in each phase remains within its solubility limit and is expressed by the enthalpy of solution term [22]. Discretization of the radial continuity equation results in

$$C_{Zr}^i = C_{Zr}^i + 2\Delta t \frac{J_+^{i-1} rc^{i-1} - J_+^i rc^i + J_-^i rc^i - J_-^{i+1} rc^{i+1}}{(r^i)^2 - (r^{i-1})^2} + s\Delta t \tag{7}$$

where rc^i is the center of mass of the radial node-i (m), r^i is the outer boundary of node-i (m), J_+^i and J_-^i are the positive and negative Zr currents (mol/m^{2}s) at node-i, respectively; s is the Zr production rate (mol/m^{3}s) due to fission and Δt is the time step (s). Fig. 4 describes the discretization scheme. The boundary conditions are that the negative current at the origin of the fuel slug is zero, and the positive current at the surface of the fuel slug is also zero, i.e., Zr cannot migrate out of the fuel.

Fig. 5a shows a comparison of the FEAST-METAL prediction with Kim et al.'s model prediction and their experimental data for U–19Pu–10Zr [19], while Fig. 5b shows a comparison of the FEAST-METAL predictions with experimental data for U–10Zr fuel [22,23]. The agreement between FEAST-METAL and the data is satisfactory.

5. Fuel–clad chemical interaction

Chemical reactions between the fuel slug and the clad material are among the most important phenomena limiting the in-pile performance of metal fuels. As a result of fuel–clad contact during steady state irradiation, the clad constituents may diffuse into the fuel and form a low-melting point alloy (eutectic). As the burnup increases, some fission products (particularly lanthanides) diffuse into the clad to form brittle phases with iron. Both mechanisms can cause clad deterioration, including breach. Fig. 6a [24] and b [6] shows that the growth rate of the interaction layer at the fuel–clad interface is proportional to the square root of time; thus, FCCI in metal fuels appears to be a diffusion-controlled process. Also, at high burnup during transients, the fuel–clad gap tends to widen due to plenum pressure and clad creep, which may cause clad wastage to stop (see high-burnup curve in Fig. 6b). However, the FCCI correlations used in the past [6,25]
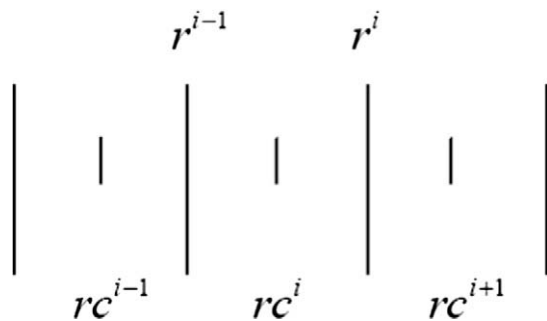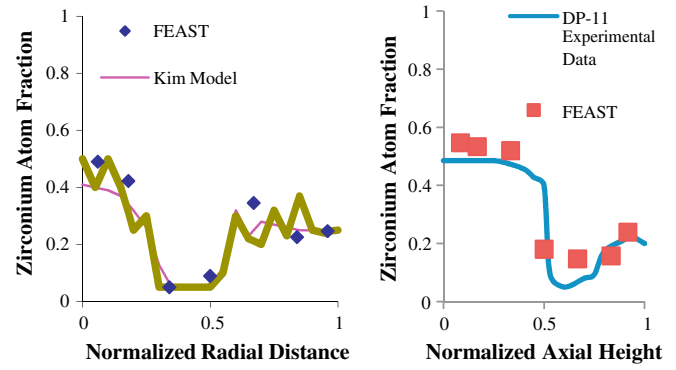

Fig. 5. Radial Zr redistribution at end of life in (a) U–19Pu–10Zr (pin T-179 in [19]), (b) U–10Zr (pin DP-11 in [22,23]).

comprise simple growth-rate vs temperature correlations, which do not account for the kinetics behavior and composition dependency correctly. Therefore, it was decided to develop a precipitation-kinetics model, inspired by physical metallurgy [26], which is described next.

5.1. Steady state FCCI

The steady-state clad wastage rate is given as:

$$\frac{dX_w}{dt} = \frac{1}{2} \frac{C_{oL} - C_{\alpha L}}{C_{\beta L} - C_{\alpha L}} \sqrt{\frac{D_L}{t}} \tag{10}$$

where X_w is the clad wastage layer thickness (m), C_{oL} the concentration of the lanthanide atoms in the fuel, $C_{\alpha L}$ the solubility limit of the lanthanides in the fuel (assumed to be zero), $C_{\beta L}$ the solubility limit of the lanthanides in the clad (its value is 0.1 [27]), t the time (s), and D_L the diffusion coefficient of lanthanides at fuel–clad interface (m^2/s) given as:

$$D_L = D_{0L} \exp\left(-\frac{Q_L}{RT}\right) \tag{11}$$

where $D_{0L} = 1350 \text{ m}^2/\text{s}$ and $Q_L = 300{,}000 \text{ J/mol}$, and T is clad inner temperature (K). The values of D_{0L} and Q_L were chosen to fit the data from the DP04 and DP11 pins (unbreached fuel pins) in the X447 irradiation in EBR-II [28]. The data from the breached fuel pins in X447 were discarded from the analysis, because their high wastage levels resulted from operation after breach. The concentration of the lanthanides in the fuel is calculated as follows:

$$C_{0L}^{t+1} = C_{0L}^t + \frac{Y_L \dot{F} \Delta t}{n_{tot}} \tag{12}$$

where C_{0L}^t is the lanthanide fractional concentration at time t, n_{tot} is the total fuel atom density (atoms/m^3), Y_L is the fission yield of the lanthanides (atom/fission), and $\dot{F}$ is the volumetric fission rate (fissions/m^{3}s) in the fuel.

5.2. Transient FCCI

A similar precipitation-kinetics model was employed for the transient scenarios, during which the dominant FCCI mechanism is eutectic formation [(U, Pu)$_6$ Fe] and liquefaction at the fuel–clad interface. The liquefaction temperature as a function of the plutonium content given in Ref. [29] was adopted in this study. The governing rate equation becomes:

$$\frac{dX_w}{dt} = \frac{1}{2} \frac{C_{0Fe} - C_{\alpha Fe}}{C_{\beta Fe} - C_{\alpha Fe}} \sqrt{\frac{D_{Fe}}{t}} \tag{13}$$

where X_w is the thickness of the clad wastage layer above the liquefaction temperature (m), C_{0FE} is the Fe concentration within the clad

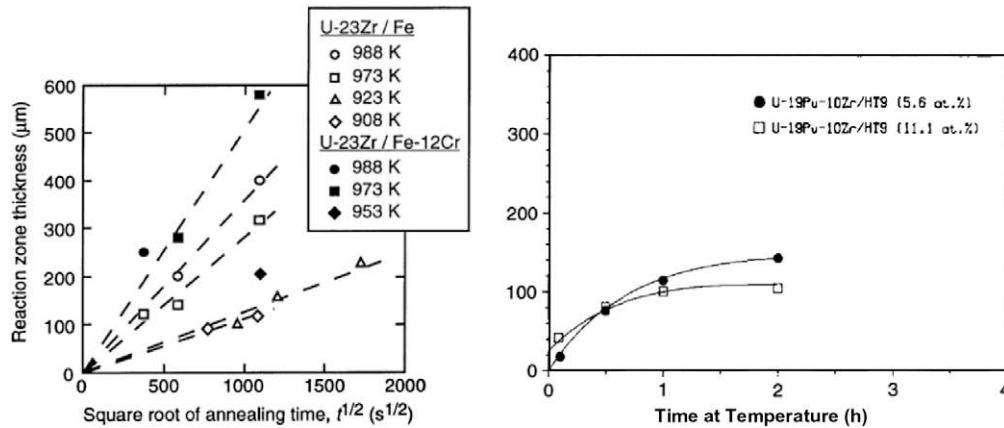**Fig. 4.** Discretization scheme to solve the radial continuity equation (Eq. (7)).

Fig. 6. Growth of the reaction zones (a) steady state growth [24], (b) transient clad penetration (μm) [6].

(=78 at.% for HT 9), $C_{\beta Fe}$ is the Fe solubility limit within the $(U, Pu)_6$ Fe layer (=14 at.%), $C_{\alpha Fe}$ is the Fe solubility limit within the clad (~zero) [24] and D_{Fe} is the Fe diffusion coefficient (m²/s), given as

$$D_{Fe} = D_{0Fe} \exp\left(-\frac{Q_{Fe}}{RT}\right) \tag{14}$$

$D_{0Fe} = 4.2 \times 10^6$ m²/s and $Q_{Fe} = 400,000$ J/mol, T is the clad inner temperature. The values of D_{0Fe} and Q_{Fe} were chosen to best fit the experimental database from furnace tests for EBR-II fuel pins [6]. The experimental data given in Ref. [6] shows that the eutectic penetration rate is weakly dependent on temperature for temperatures below 750 °C; hence, in FEAST-METAL, if the clad inner temperature is above the eutectic temperature but below 750 °C, the diffusion coefficient calculated at 750 °C is used to predict the reaction rate. Finally, it is assumed that FCCI ceases if the fuel–clad gap widens to 50 μm, consistent with the experimental observations in Ref. [6]. Table 2 shows the comparison between the precipitation-kinetics model predictions and data, where the predictions from the empirical clad-wastage correlation in Ref. [6] are also reported. Note that for the long transient data point (12 h), the empirical correlation overestimates the clad wastage very significantly, as it cannot reproduce the diffusion-like behavior.

6. Mechanical analysis

The stress–strain analysis module in FEAST-METAL adopts the LIFE algorithm [30] with a 1D finite difference solution. This approach accounts for thermal expansion, elastic, thermal and irradiation creep, plasticity and swelling strains. The code solves the mechanical-equilibrium equation with the generalized plain strain approach, by imposing that the radial displacement and radial stress are continuous at the spatial node interfaces. Furthermore, the axial force balance is also applied to calculate the axial strain (if the gap is open) or the axial friction force (if the gap is closed, and thus the clad and fuel are 'locked' together). If eutectic liquefaction occurs at the fuel–clad interface, the friction force is set equal to zero at the corresponding axial location; hence, the fuel is allowed to move upwards freely in this case, if there is no other locked node above. The metal fuel creep equations given in Ref. [31] were adopted in FEAST-METAL. The fuel plastic behavior is modeled according to the so-called 'perfectly plastic' approach [32]. The fuel swelling strain (ϵ^s) is given as

$$\varepsilon^s = \frac{1}{3}\left[\left(\frac{\Delta V}{V}\right)_{\substack{Solid\\FP}} + \left(\frac{\Delta V}{V}\right)_{\substack{Closed\\Bubble}} + \left(\frac{\Delta V}{V}\right)_{\substack{Open\\Porosity}} - \left(\frac{\Delta V}{V}\right)_{\substack{Hot\\Pressing}}\right] \tag{15}$$

Fuel swelling is assumed to be isotropic within the fuel. Hence, one-third of the total volumetric swelling is assigned to each direction. Solid-fission product swelling is assumed to be 1.5%/at.% burnup as given in Ref. [9]. The swelling due to the closed bubbles and open porosity is calculated with the GRSIS algorithm, described in Section 3 above. The hot-pressing contribution to fuel swelling is due to FCMI, and is negative. That is, when the initial gap space between the fuel and the clad is filled with the swollen fuel slug, further gas swelling is restrained by the clad. The volume of the existing open pores decreases, so that further buildup of the solid and liquid fission products is accommodated. FCMI remains at a low level as long as enough open porosity is available (>10%). The mechanism is assumed to be creep-dependent [9].

In the clad, the swelling strain is due solely to void formation given for each direction as:

$$\varepsilon_s^{clad} = \frac{1}{3}\left(\frac{\Delta V}{V}\right)_{\substack{Void\\Swelling}} \tag{16}$$

Table 2
Transient clad wastage data for EBR-II furnace tests [6] and model predictions.

Test	Temperature (°C)	Burnup (at.%)	Time (h)	Experimental data (μm)	Precipitation-kinetics model (μm)	Empirical correlation (μm)
1	675	10.8	12	140	168	277
2	700	9.8	1.0	58, 76[a]	63	54
3	740	11.3	1.0	58, 87[a]	63	85
4	770	9.6	1.0	80	76	122
5	800	10.8	0.1	42	50	36
6	800	11.3	0.5	79	100	98
7	800	10.0	1.0	100	127	130
8	800	10.5	2.0	104	127	130

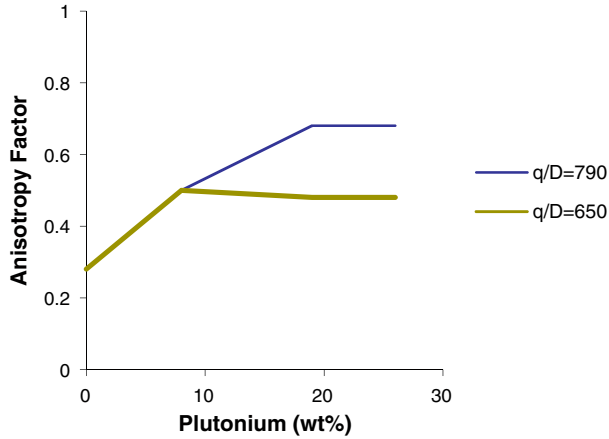[a] The test was performed for two different samples at the same transient temperature.

Fig. 7. Anisotropy factor.

For HT 9, void swelling level remains low at doses as high as 200 dpa [33].

6.1. Anisotropic fuel slug deformation

The empirical approach reported in Ref. [9] is adopted in FEAST-METAL, to model anisotropic deformation of the metal fuel slug prior to fuel–clad contact. The anisotropy is due to the formation of large radial cracks in the brittle ternary U–Pu–Zr fuel. In U–Zr fuels, tearing at the grain or phase boundaries in the outer region of the fuel slug also occurs due to anisotropic irradiation growth of α-U crystals. To incorporate these effects, an effective fuel slug radius is introduced:

$$r^{eff} = r_o + dr_{slug} + dr_{crack} = r_{slug} + dr_{crack} \qquad (17)$$

where r_o is the as-fabricated slug radius and dr_{slug} is the radial displacement due to thermal expansion, elasticity, creep/plasticity, closed-bubble, open-pore and solid-fission product swelling. The increment dr_{crack} is due to the cracks and tearing. After the slug comes in contact with the clad, further fuel swelling is accommodated by the closure of the tears and cracks. This process prevents Fuel–Clad Mechanical Interaction (FCMI) from growing at first. During this stage of fuel–clad contact, the contact area continues to increase without significant FCMI stress, while the fuel slug and the clad are axially locked. According to this description, the fuel–clad contact process can be divided into three time intervals:

(I) $r^{eff} < r^i$: no restraint by the clad (no contact)
(II) $r^{slug} < r^i = r^{eff}$: axial restraint by the clad, no radial restraint
(III) $r^i = r^{slug}$: both axial and radial restraint by clad

Table 3
Fuel-slug axial elongation.

Fuel composition	Fuel smear density (%)	$\frac{q}{D}$ (W/cm²)	Axial elongation (%)	
			Experimental data	FEAST predictions
U–10Zr	76 [35]	790	6.2	6.0
U–19Pu–10Zr	76 [35]		1.5	1.8
U–10Zr	72 [34]	830	8.5	7.2
U–8Pu–10Zr	72 [34]		6.5	5.7
U–19Pu–10Zr	72 [34]		2.5	2.3
U–10Zr	75 [4]	650	8	9.0
U–8Pu–10Zr	75 [4]		5.8	6.1
U–19Pu–10Zr	75 [4]		6.5	6.6

r^i is the inner radius of the clad.

$$dr^{crack} = f^{crack} r_o^{gap} \qquad (18)$$

where r_o^{gap} is the as-manufactured gap width. The anisotropy factor, f^{crack} was calculated based on references [4,34,35] as a function of Pu content and $\frac{q}{D}$ (average linear power divided by the diameter of the slug), and is given in Fig. 7. Note that the value of f^{crack} 'saturates' above 19 wt.% Pu and 790 W/cm² $\frac{q}{D}$ value. Table 3 reports axial elongation prediction from this model, which are in reasonable agreement with the experimental data.

7. Transient creep-fracture model for the clad

During transients in which the clad temperatures rise significantly, intergranular creep fracture may become the dominant clad failure mechanism. A popular approach to predict clad rupture in fast reactor analysis is the simple Cumulative Damage Fraction (CDF) model [36], which combines creep fracture data collected at fixed temperature and stress, to predict failure for situations where the temperature and stresses change continuously with time. In FEAST-METAL the user has the option to choose the CDF model; however, during transients the stress and temperature may change very rapidly, which makes the use of the CDF approach open to questions. Therefore, it was decided to introduce a more mechanistic creep-fracture model that is based on the constrained diffusional cavity growth mechanism [37]. Intergranular creep fracture can occur by nucleation and growth of grain boundary cavities [38]. The idea of the original model was to track the radius of the cavities up to the point of cavity coalescence. However, this approach tended to overestimate the failure times significantly [38]. The idea adopted here is again to track the radius of the cavities within the clad; however, when the radius reaches a critical value, which depends on temperature and stress, it is assumed to propagate instantaneously, thus breaching the clad. An expression for the cavity radius growth rate for multi-axial loading is [38].

$$\frac{da}{dt} = \frac{\sigma_I^\infty - (1-w)\sigma}{h(\psi)a^2 \left[\frac{q(w)kT}{2\Omega\partial D_b} + \frac{q'\sigma_{eq}}{\dot{\varepsilon}_{eq}\lambda^2 d}\right]} \qquad (19)$$

with $q(w) = -2 \ln w - (3-w) \times (1-w)$, $h(\psi) = \frac{1}{\sin\psi}\left[\frac{1}{1+\cos\psi} - \frac{\cos\psi}{2}\right]$, $w = \frac{(2a)^2}{\lambda^2}$, $\cos\psi = \frac{\gamma_b}{2\gamma_s}$, $\sigma_0 = \frac{2\gamma_s \sin\psi}{a}$, $q' = \pi\left(1 + \frac{3}{n}\right)^{0.5}$, where d is the grain boundary diameter, σ_I^∞ is the applied hoop stress, σ_{eq} the Von-Mises equivalent stress, σ_0 the sintering stress (the stress state at which the internal force due to surface tension is balanced by the external forces), a the cavity radius, and $\dot{\varepsilon}_{eq}$ the equivalent creep strain rate, T is the temperature in Kelvin. All other parameters in these equations are reported in Table 4.

The model was applied to HT 9 for fixed temperature and stress, for which time-to-failure data are available [39]. Therefore, it was possible to generate a lookup table for the critical cavity radius (Table 5). Then the table can be used for any transient as follows: when Eq. (19) predicts a cavity size equal to the critical cavity radius corresponding to the instantaneous value of the stress and

Table 4
Parameters used in the FEAST-METAL transient creep-fracture model [38].

n	5
Ω (m³)	1.18E−29
∂D_b (m³/s)	1.1E−12
Q_b (J/mol)	1.74E+5
γ_s (J/m²)	2.1
γ_b (J/m²)	0.85
d (m)	20E−06
λ (m)	7E−06
k (J/K)	1.38E−23

Table 5
Critical crack radius (in μm) for HT 9.

Hoop stress (MPa)	Temperature (°C)					
	675	700	725	750	800	870
10	33.5	10.89	6.854	4.599	1.299	3.418
25	3.863	2.589	1.923	1.577	0.788	1.753
50	2.756	1.533	1.052	0.677	0.668	0.903
75	1.599	1.083	0.687	0.397	0.397	0.384
100	1.272	0.795	0.456	0.247	0.219	0.155
125	1.001	0.572	0.312	0.166	0.114	0.0
150	0.767	0.417	0.226	0.120	0.051	0.0
175	0.587	0.315	0.170	0.090	0.0	0.0
200	0.458	0.246	0.134	0.070	0.0	0.0

temperature, the clad is assumed to fracture. The lookup table approach can be replaced by actual critical cavity radius data, if they become available.

8. Validation of FEAST-METAL

8.1. Steady state

The FEAST-METAL predictions were compared to the EBR-II reactor irradiation database, and to the predictions of the ALFUS and LIFE-METAL codes, when available. The EBR-II test assemblies designated as X425 [9,34,40,41], X430 [35] and X447 [23,28] were used for the validation exercise, as sufficient information is available for these assemblies.

8.1.1. X425 assembly

X425 is one of the most successful irradiation performed in EBR-II. Table 6 shows the fuel geometry, composition and operating conditions at the beginning of life.

Table 6
Fuel data for EBR-II assemblies.

| Parameter	Value		
Fuel assembly	X425	X430	X447
Fuel composition	U–19Pu–10Zr	U–19Pu–10Zr	U–10Zr
Clad material	HT 9	HT 9	HT 9
Fuel slug radius (mm)	2.16	2.86	2.20
Clad inner radius (mm)	2.54	3.28	2.54
Clad outer radius (mm)	2.92	3.68	2.92
Fuel smear density (%)	72.3	76	75.0
Fuel active length (cm)	34.3	34.3	34.3
Plenum to fuel ratio	1.0	1.4	1.4
Peak linear heat rate (kW/m)	40	50	33
Peak clad temperature (°C)	590	590	660
Peak fast flux (n/cm²/s)	2.3×10^{15}	1.6×10^{15}	1.9×10^{15}
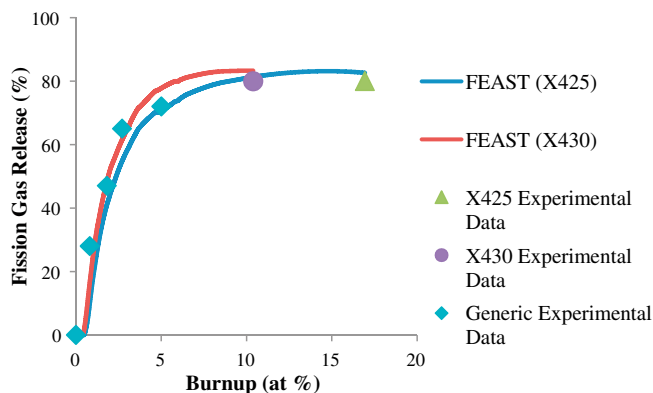
Fig. 8. Fission gas release behavior of the X425 and X430 fuel rods.

The fission gas release for the X425 peak fuel rod at the end of life [34] along with generic data for U–19Pu–10Zr fuel from [17] is shown in Fig. 8. The agreement between data and predictions is excellent.

The clad strain profile at 15.8 at.% peak burnup predicted by FEAST is compared to the ALFUS predictions and the experimental data in Fig. 9. Both codes give reasonable results, with FEAST-METAL predicting the correct bottom-peaked profile and a closer peak clad strain. The metal fuel slug is rather stiff in the bottom region due to the combined effect of lower temperature and lower amount of open porosity; thus, FCMI is significant. On the other hand, the upper part of the fuel is softer and compliant and the resulting clad strain is relatively low.

A comparison of the FEAST, ALFUS and also LIFE-METAL predictions with respect to the experimental data is reported in Table 7. Note that the perfect agreement of LIFE-METAL with the experimental data is due to the fact that X425 (and X441) were used for calibration of the various empirical coefficients in that code.

8.1.2. X430 assembly

The fuel composition and geometry for the X430 assembly are reported in Table 6. The peak assembly burnup is 11.9 at.%. The fission gas release for the X430 peak fuel rod at the end of life [35] along with generic data for U–19Pu–10Zr fuel from [17] is shown in Fig. 8. The agreement between data and predictions is again very good. Also, the FEAST predictions reproduce the clad strain data reasonably well, as shown in Table 8.

8.1.3. X447 assembly

The fuel specifications for the X447 assembly are reported in Table 6. Note that the X447 clad temperature is quite high. For HT 9, thermal creep becomes very significant in this temperature range, and it has a strong dependency on temperature. FEAST has an option to divide the axial node at the top of the fuel into four sub-nodes, to get a more detailed distribution of the clad strain, the clad failure time and clad wastage for high temperature operations and transient scenarios. The fission gas release at the end of life for the X447 fuel assembly is shown in Fig. 10 and is about 72–76% [28]. The FEAST prediction for the peak fuel rod (DP-04) is 75%. Fig. 10 also shows generic data for U–10Zr at lower burnup from Ref. [17]; predictions and data are again in good agreement. The clad strain for the DP-04 fuel rod [28] is also reproduced well by FEAST, as shown in Fig. 11.

8.2. Transients

The transient capabilities of FEAST-METAL were evaluated using the database from the pin furnace tests performed at the Argonne National Laboratory [36,42]. The experiments were performed at the ANL alpha-gamma hot cell facility, which features a radiant furnace with computer-controlled temperature, able to
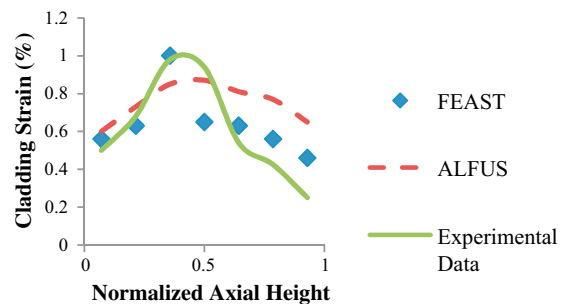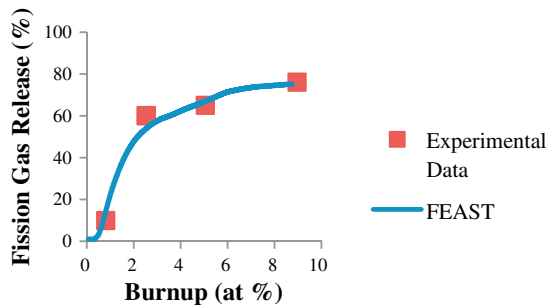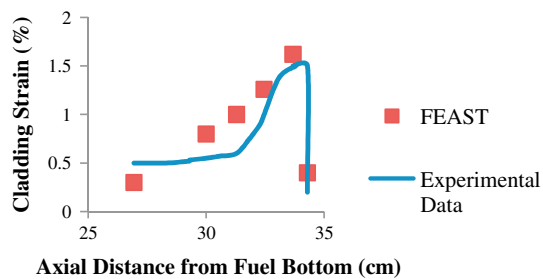

Fig. 9. X425 axial distribution of clad strain at peak burnup 15.8 at.%.

Table 7
X425 peak clad strain (%).

Peak burnup (at.%)	Experimental data	FEAST		ALFUS [9]		LIFE-METAL [41]	
		Clad strain (%)	Relative error (%)	Clad strain (%)	Relative error (%)	Clad strain (%)	Relative error (%)
10.4	0.25	0.22	−12.0	∼0.37	48	∼0.25	0.0
15.8	0.98	1.0	2.0	∼0.86	−14	∼0.98	0.0
18.9	2.0	2.23	11.5	∼1.55	−22.5	∼2.4	20

Table 8
X430 assembly peak clad strain at end of life (11.9 at.%).

Fuel rod ID	Burnup (at.%)	Experimental data	FEAST prediction	Relative error (%)
T-654	11.6	0.97	0.87	−10.3
T-655	11.8	0.86	0.93	8.1
T-659	11.7	1.17	1.04	−11.1
T-660	11.9	1.03	1.19	15.5

Fig. 10. Fission gas release for X447 assembly (DP-04 rod).

Fig. 11. Peak clad strain for X447 assembly (DP-04 rod).

these fuel pins prior to furnace testing has not been published. Therefore, in the FEAST-METAL analyses it was assumed that the irradiation history is the same as the peak X425 fuel rod. Although the database has some variety in burnup and plenum-to-fuel ratio, plutonium content and test temperature, the number of tests is very limited. Therefore, it was decided to do also a code-to-code comparison of FEAST-METAL with LIFE-METAL and the FPIN2 code.

Table 10 shows the predictions and the experimental data for the failure time, clad wastage and peak clad strain. Failure time predictions are performed according to the Cumulative Damage Fraction (CDF) method (top value) and constrained diffusional cavity growth model (bottom value) (see Section 7 for the description of these models), the latter giving somewhat more conservative predictions. LIFE-METAL and FPIN code predictions were performed with the CDF method. Given the uncertainty in the irradiation history, the FEAST predictions for FM1, FM3, FM5 and FM6 are in reasonable agreement with the data. Note that FM1 and FM2 are very similar fuel pins, with a difference in Pu concentration, which is not likely to cause a very significant difference in irradiation and transient performance. FEAST errs on the conservative side for the FM1 and FM2 tests, as far as failure time is concerned. The FM4 test is an odd case: during the test, ballooning of the plenum region was observed [36]. None of the codes could predict this behavior. It is hypothesized that plenum ballooning resulted in decreased plenum pressure, so clad breach was delayed significantly compared to the code predictions [36]. The clad wastage predictions of FEAST are also reasonably good. As for clad strain, it would not be appropriate to judge the accuracy of the codes from their performance for the failed pins (FM1 through FM4), because in these cases significant straining occurs during rupture, which is captured by the PIE measurements, but not by the codes. On the other hand, for the pins with no failure (FM5 and FM6), the FEAST-METAL predictions are reasonably close to the data, and actually a bit conservative.

heat intact irradiated fuel pins to the point of clad breach. Key pin parameters and test conditions are summarized in Table 9. FM-1, 2, 3, 4 and 6 are ramp-and-hold tests while FM-5 is a ramp-and-cool test. FM-5 was performed to simulate the worst possible Loss of Flow Accident in EBR-II. Unfortunately, the irradiation history of

Table 9
Key furnace-test pin parameters.

Test no.	Fuel type	Plenum to fuel ratio	Burnup (at.%)	Test temperature (°C)	Test duration (min)
FM1	U–10Zr/HT 9	1.0	3	820	67
FM2	U–19Pu–10Zr/HT 9	1.0	3	820	112
FM3	U–26Pu–10Zr/HT 9	1.4	2.2	820	146
FM4	U–19Pu–10Zr/HT 9	1.5	11.4	770	68
FM5	U–19Pu–10Zr/HT 9	1.5	11.4	Ramp to 780; cool	3
FM6	U–19Pu–10Zr/HT 9	1.0	11.3	650–670	2160

Table 10
Furnace test data and code predictions.

Test	Failure time (min)				Clad wastage (%)				Peak strain (%)			
	FPIN	LIFE	FEAST	TEST	FPIN	LIFE	FEAST	TEST	FPIN	LIFE	FEAST	TEST
FM1	36	79	69	67	30	53	51	64	6.0	1.1	0.7	3.3
			58				47				0.5	
FM2	42	75	5648	112	37	50	45	67	6.0	1.0	0.7	2.3–4.3
							42				0.5	
FM3	108	217	129	146	86	50	70	65	6.0	1.0	0.7	1.2
			110				64				0.4	
FM4	16	9	12	68	8.2	3	10	24	15.0	0.7	0.4	10–15
			10				10				0.3	
FM5	No failure	No failure	No failure	No failure	0.15	Z0	5.0	0	0.6	0.0	0.2	0.1
			No failure				5.0					
FM6	222	1320	No failure	No failure	0.0	0.0	5.0	0	4.5	1.0	1.0	0.89
			No Failure				5.0					

9. Conclusions

A new computer code, FEAST-METAL, was developed to predict the steady and transient behavior of metallic fuel alloys in sodium fast reactors. Attractive/novel features of FEAST-METAL with respect to other metal–fuel codes include a flexible structure that allows for easy integration of constitutive models for new metal fuel alloys and clad materials, the ability to account for the variation of material properties (fuel creep, thermal expansion, Young's modulus) with the phases locally present in the fuel, a mechanistic fission gas release and swelling model originally developed for metal fuel, a FCCI model based on precipitation kinetics, a fuel constituent redistribution model based on thermo-transport theory, and a transient clad creep-fracture model based on the constrained diffusional cavity growth mechanism. FEAST-METAL is meant to be a robust engineering code with the most advanced mechanistic (but macroscopic) models, to be used in guiding the development of advanced metal fuels, in pre-irradiation calculations and scoping studies of novel fast reactors.

The code performance was validated against the available EBR-II database for steady state and furnace (transient) tests. The steady-state and transient tests encompassed a burnup range of 7–19 at.% and 2–11 at.%, respectively, corresponding to peak clad doses up to 100 dpa. The peak clad temperature for the steady state and transient tests were in the 550–660 °C and 650–820 °C, respectively. A comparison of data and code predictions for these tests suggests that FEAST-METAL is able to predict important phenomena such as clad strain, fission gas release, clad wastage, clad failure time and axial fuel slug deformation, satisfactorily. However, more data are needed for a statistically-significant, quantitative assessment of the code capabilities.

Acknowledgements

Appendix A

The Appendix reports the fundamental data used to calculate the zirconium radial distribution within the metal fuel slug.

A.1. Enthalpy of solution

The enthalpy of solution of Zirconium in α and β phases is negligible. On the other hand, the enthalpy of solution of the γ and δ matrix phases is given as follows:

$$\Delta \overline{H}_s = G_{Zr}^E - T \frac{\partial G_{Zr}^E}{\partial T} \tag{A.1}$$

$$G_{Zr}^E = x_U^2 (43764.5 - 22T - 44174.7 x_{Zr} + 38635.1 x_{Zr}^2) + x_{Pu}^2 (6574.7) + x_U x_{Pu} (15884) \tag{A.2}$$

where $\Delta \overline{H}_s$ is the enthalpy of solution (J/mol), G_{Zr}^E the free energy of Zirconium (J/mol), x_U the Uranium mole fraction, x_{Zr} the Zirconium mole fraction, x_{Pu} the Plutonium mole fraction and T is the temperature (K).

A.2. Effective heat of transport

Note that the effective heat of transport values (see Table A.1) are linearly interpolated between their values for the U–Zr and U–8Pu–Zr alloys. For plutonium concentrations above 8 wt.%, it is assumed that the effective heat of transport values stay constant.

A.3. Effective diffusion coefficients

The diffusion coefficient is defined as follows:

$$D = D_o \exp\left(-\frac{Q}{RT}\right) \tag{A.3}$$

Q is the activation energy and D_o is the diffusion constant. They are given in Tables A.2 and A.3.

The Zr diffusion coefficient for the dual phase $\beta + \gamma$ is calculated by the diffusion constant of the β and γ phases from Table A.2

Table A.1
Effective heat of transport (kJ/mol).

Phase	U–>8Pu–Zr	U–Zr
α	200	0.0
δ	160	0.0
β	450	0.0
γ	−200	−150

Table A.2
Diffusion coefficients for U–Zr alloy phases.

Phases	D_o (m²/s)	Q (kJ/mol)
α	2×10^{-7}	170
δ	2×10^{-7}	150
β	5.7×10^{-5}	180
γ	$10^{(-5.1 - 8.05 x_{Zr} + 9.13 x_{Zr}^2)}$	$128 - 107 x_{Zr} + 174 x_{Zr}^2$

Table A.3
Diffusion coefficients for U–Pu–Zr alloy phases (Pu is >8 wt.%).

Phases	D_o (m^2/s)	Q (kJ/mol)
α	2×10^{-6}	170
δ	2×10^{-6}	150
β	4.0×10^{-4}	180
γ	$10^{(-5.1-8.05x_{Zr}+9.13x_{Zr}^2)}$	$128 - 107x_{Zr} + 174x_{Zr}^2$

multiplied by a factor of 10 depending on whether the β or γ phase fraction exceeds 50%, respectively.

References

[1] US DOE Nuclear Energy Research Advisory Committee and The Generation IV International Forum, A Technology Roadmap for Generation IV Nuclear Energy Systems, US Department of Energy, Report, December 2002.
[2] US Department of Energy, Global Nuclear Energy Partnership Strategic Plan, US Department of Energy, Report No. GNEP-167312, Rev. 0, 2007.
[3] G.L. Hofman, L.C. Walters, T.H. Bauer, Progress in Nuclear Energy 31 (1997) 83–110.
[4] G.L. Hofman, R.G. Pahl, C.E. Lahm, D.L. Porter, Metallurgical Transactions A 21A (1990) 517–528.
[5] J.R. Matthews, T. Preussers, Nuclear Engineering and Design 101 (1987) 281–303.
[6] B. Cohen, H. Tsai, L.A. Neimark, Journal of Nuclear Materials 204 (1993) 244–251.
[7] M.C. Billone, Y.Y. Liu, Status of the fuel element modeling codes for metallic fuels, in: Proceedings of the International Conference Reliable Fuels for Liquid Metal Reactors, American Nuclear Society Tucson, Arizona 1986.
[8] T. Kobayashi, M. Kinoshita, S. Hattori, T. Ogawa, Y. Tsuboi, M. Ishida, S. Ogawa, H. Saito, Nuclear Technology 89 (1990) 183–193.
[9] T. Ogata, T. Yokoo, Nuclear Technology 128 (1999) 113–123.
[10] W. Hwang, N. Cheol, B.S. Thak, Y.C. Kim, Nuclear Technology 123 (1998) 130–141.
[11] J. Carmack, K.O. Pasamehmetoglu, Review of Transmutation Fuel Studies, Idaho National Laboratory Report, INL/EXT-08013779, 2008.
[12] T.H. Bauer, J.W. Holland, Nuclear Technology 110 (1995).
[13] S. Hu, C.H. Henager, H.L. Heinisch, M. Stan, M.I. Baskes, M.S. Valone, Journal of Nuclear Materials 392 (2009) 292–300.
[14] <http://www.pnl.gov/frapcon3/>.
[15] S.C. Chapra, R.P. Canale, Numerical Methods for Engineers, McGraw-Hill International Editions, 1998.
[16] A. Karahan, J. Buongiorno, M.S. Kazimi, Modeling of Thermo-Mechanical and Irradiation Behavior of Metallic and Oxide Fuels for Sodium Fast Reactors, Report No: MIT-NFC-TR-110, Center for Advanced Nuclear Energy Systems, Massachusetts Institute of Technology, 2009.
[17] C.B. Lee, D.H. Kim, J.H. Youn, Journal of Nuclear Materials 288 (2001) 29–42.
[18] W.G. Steele, A.R. Wazzan, D. Okrent, Nuclear Engineering and Design 113 (1989) 289–295.
[19] Y.S. Kim, S.L. Hayes, G.L. Hofman, A.M. Yacout, Journal of Nuclear Materials 359 (2006) 17–28.
[20] M. Ishida, T. Ogata, M. Kinoshita, Nuclear Technology 104 (1993) 37–51.
[21] W. Hwang, B. Lee, J.Y. Kim, Annals of Nuclear Energy 27 (2000) 1059–1069.
[22] G.L. Hofman, S.L. Hayes, M.C. Petri, Journal of Nuclear Materials 227 (1995) 277–286.
[23] C. Nam, W. Hwang, D. Sohn, Statistical failure analysis of metallic fuel U–10Zr/HT 9 fast reactor fuel pin by considering the weibull distribution and cumulative damage fraction, vol. 25, Annals of Nuclear Energy, 1998, pp. 1441–1453.
[24] K. Nakamura, T. Ogata, M. Kurata, A. Itoh, M. Akabori, Journal of Nuclear Materials 275 (1999) 246–254.
[25] T. Yokoo, T. Ogata, H. Ohta, Journal of Nuclear Science and Technology 37 (8) (2000) 636–645.
[26] W.F. Hosford, Physical Metallurgy, Taylor & Francis, 2005.
[27] P.C. Tortorici, M.A. Dayananda, Journal of Nuclear Materials 204 (1993) 165–172.
[28] R.G. Pahl, C.E. Lahm, S.L. Hayes, Journal of Nuclear Materials 204 (1993) 141–147.
[29] K. Nakamura, T. Ogata, M. Kurata, M.A. Mignanelli, Journal of Nuclear Science and Technology 38 (2) (2001) 112–119.
[30] D.R. Olander, Fundamental Aspects of Nuclear Reactor Fuel Elements, US DOE, 1976.
[31] E.E. Gruber, J.M. Kramer, Gas bubble growth mechanisms in the analysis of metal fuel swelling, in: Proceedings of 13th International Symposium (Part-I) Radiation Induced Changes in Microstructure, ASTM-STP-955, 1987, p. 432.
[32] P. Hovel, G. Kozyreff, J. Ockendon, Applied Solid Mechanics, Cambridge University Press, 2009.
[33] M.B. Toloczko, F.A. Garner, C.R. Eiholzer, Journal of Nuclear Materials 212–215 (1) (1994) 604–607.
[34] R.G. Pahl, R.S. Wisner, M.C. Billone, G.L. Hofman, Steady-state irradiation testing of U–Pu–Zr fuel >18 at.% burnup, in: Proceedings of the 1990 International Fast Reactor Safety Meeting, vol. 4, 1990, pp. 129–137.
[35] D.C. Crawford, S.L. Hayes, R.G. Pahl, Transaction of American Nuclear Society 71 (1994) 178–179.
[36] J.M. Kramer, Y.Y. Liu, M.C. Billone, H.C. Tsai, Journal of Nuclear Materials 204 (1993) 203–211.
[37] H. Reidel, Zeitschrift fuer Metallkunde 76 (1985) 669–675.
[38] G. Eggeler, J.C. Earthman, N. Nilsvang, B. Llschner, Acta Metallurgica 37 (1989) 49–60.
[39] R.J. DiMelfi, E.E. Gruber, J.M. Kramer, Strength and rupture-life transitions caused by secondary carbide precipitation in HT 9 during high temperature low-rate mechanical testing, in: First International Conference on Microstructures and Mechanical Properties of Aging Materials, 1993, pp. 187–196.
[40] R.G. Pahl, Journal of Nuclear Materials 188 (1992) 3–9.
[41] R.G. Pahl, C.E. Lahm, H. Tsai, M.C. Billone, Irradiation experience with HT 9 Clad Metallic Fuel, ANL/CP-72040, 1992.
[42] Y.Y. Liu, Journal of Nuclear Materials 204 (1993) 194–202.